Particle Image Velocimetry investigation of the aerodynamic interaction between helicopter and an aircraft carrier

R. Bardera, J.C. Matías*, E. Barroso

National Institute for Aerospace Technology (INTA), Spain
* Correspondent author: matiasgjc@inta.es

Keywords: PIV, Helicopters, Velocity fields

ABSTRACT

Helicopters greatly expand operational capabilities during military missions at the sea. The aircraft carriers are capable of accommodating fixed-wing and rotary-wing aircraft operations. They not only have one runway for take-off, but also have different spots for helicopter operations. As they are spread over the deck of the aircraft carrier, the non-aerodynamic geometries of the take-off ramp and the island can generate complex flows, with high velocity gradients and turbulence intensities that can make complex the helicopter landing and take-off maneuvers for pilots. This study analyses the interaction between the aerodynamic patterns generated by the warship and those generated during the operation of the helicopter. Two wind conditions are simulated: headwind and crosswind. The results are provided by a Particle Image Velocimetry (PIV) system installed at the wind tunnel test section of a low-speed wind tunnel. The model of aircraft carrier and helicopter are tested in a reduced scale of 1:100. And the helicopter rotor rotates at sufficient speed to ensure the similarity of the thrust coefficient with the real case. Finally, during the wind tunnel tests, using an automatic positioning system, the helicopter is placed in different positions above the aircraft carrier flight deck in order to obtain PIV images and extract non-dimensional velocity contours with and without the helicopter effect. The results have shown important effects of the aerodynamics generated by the bow, the hull and the aircraft carrier island, with velocity differences up to 70 % depending on the landing spot analyzed.

1. Introduction

The main feature of helicopters is the possibility to hover in close proximity to objects and structures, helping during military operations and rescue missions. Nevertheless, performing such helicopter operations becomes highly complex for pilots when they have to hover close to structures like buildings [1], oil rigs [2], military frigates [3], or aircraft carriers [4]. The inherent challenge arises from the fact that these non-aerodynamic structures induce flow detachments, high velocity gradients, and turbulence intensities, all of which can directly impact helicopter stability. Modern military operations often use aircraft carriers to support missions at sea in close proximity to conflict zones without infrastructure. Then, the use of helicopters in combination

with aircraft carriers becomes imperative, and demands risky aircraft operations conducted in immediate proximity to the structures of the warship.
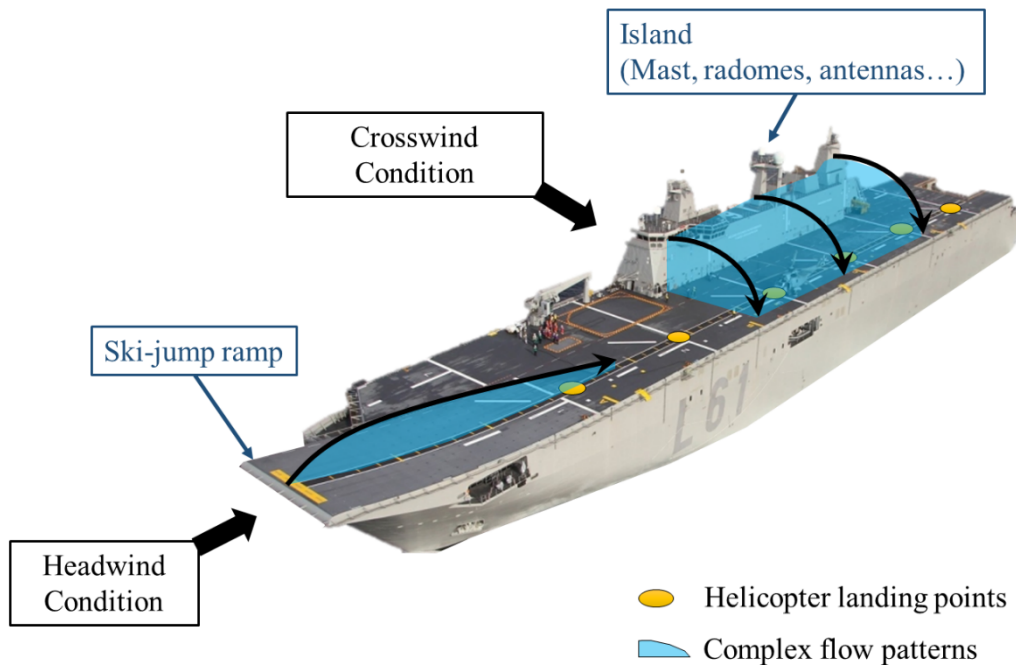

Figure 1. Ship-generated flow patterns that can affect the helicopter landing spots.

Hovering inside these turbulent flows generated by warships requires precise pilot adjustments to control the aircraft, consequently elevating the pilot's workload. Research performed by Lee and Zan [5, 6] has underscored that low-frequency oscillations within the range of 0.2 to 2 Hz are the major influences on the proper helicopter operation. Consequently, different studies has been undertaken to describe the airflow around military vessels [7-14]. These investigations include diverse aspects such as the characterization of the air wake structure [7, 8], both numerical and experimental simulations evaluating the wake unsteadiness [9-11], velocity data analysis [12, 13], and turbulent flow measurements within the wake [14]. There are also Computational Fluid Dynamics (CFD) models that represents the dynamic interference between helicopters and ships [15] or the behavior of a hovering rotor in close proximity to ship structures [16]. Another way of exploration involves extracting experimental data from wind tunnel tests, where Particle Image Velocimetry (PIV) is employed to capture velocity measurements, providing data of the airwake around the ship and the helicopters rotor downwash flow field [5, 17, 18]. Another alternative for wind tunnel tests is to use balances to quantify aerodynamic forces and moments [19-23]. For instance, studies on the interference between a CH-46 tandem helicopter and V-22 tilt-rotors in a shipboard environment are presented in [19, 20]. Similarly, Wang et al. adopted a comparable approach to assess the aerodynamic impact of a ship superstructure during helicopter operations

[21, 22]. Their methodology involved the utilization of AirDyn, a six-component dynamic force balance mounted on a 1/54th scale helicopter, specifically designed for water tunnel force measurements.

Assessing the impact of the flow field on pilot workload can be obtained from pilot's feedback during training exercises in high-fidelity helicopter flight simulators [24-28, 29, 30]. For instance, in [24] there is a frequency-domain analysis of stick movements that suggests that the atmospheric boundary layer affects the controls within the 0.1–2 Hz range. The simulators also reveal how various factors such as motion cues, airwake conditions, and ship motion states significantly influence the overall workload of the pilot [25]. Additionally, an investigation into the impact on pilot workload and handling qualities during shipboard recovery operations is available in [30]. This study utilizes the flight simulator results along with four real experimental tests conducted under diverse environmental conditions.

Concerning aircraft carriers, the unsteady airflow have been analyzed on a generic geometries of aircraft carrier [31] or above real design warships [32, 26]. Notably, the aerodynamics above the flight deck can be significantly influenced by elements such as the ski-jump ramp and the island, potentially posing risks to take-off operations [33]. This is also shown in the computational and experimental findings of the HMS Queen Elizabeth aircraft carrier [32]. The same researchers have also a piloted flight simulation aimed at investigating helicopter recovery operations above the carrier deck under different wind conditions [26].

The present study focuses on the aircraft carrier illustrated in Figure 1. Its total length is 230 m and the beam 32 m and has a take-off runway for fixed wing operations and helicopter landing spots distributed above the deck as marked in yellow in Figures 1 and 2. As the warship incorporates a ski jump ramp, and the superstructure comprises an island composed with antennas, masts, and radomes, the aerodynamics above the aircraft carrier deck are susceptible to influences from either the ski jump ramp under headwind conditions or the superstructure under crosswind conditions (Figure 1). The intricate and non-stationary flow patterns surrounding the ship present a challenge that can impact helicopter operations during take-off or landing maneuvers [34-36]. Figure 2 details the exact positions of the helicopter landing spots analyzed in this study. Moreover, the typical approach of the helicopter to the aircraft carrier involves following a designated landing path, exemplified by landing spot 6, where the helicopter consistently aligns its front with the bow of the warship.

The main goal of this paper is to show the aerodynamic interaction between the flow patterns generated by the aircraft carrier and the helicopter rotor operating above the flight deck. For this purpose, wind tunnel tests with scaled aircraft carrier and helicopter models are performed and Particle Image Velocimetry (PIV), to extract flow patterns and velocity data with and without the

helicopter on the landing spots, simulating headwind and crosswind conditions. This work is part of an internal project about the interaction between warships and helicopters aerodynamics developed at the National Institute for Aerospace Technology (INTA) in Spain, with previously published papers about the aerodynamics around the aircraft carrier [36], aircraft carrier flow control [33, 37], and helicopter internal force measuring system HELIBAL [38-39].
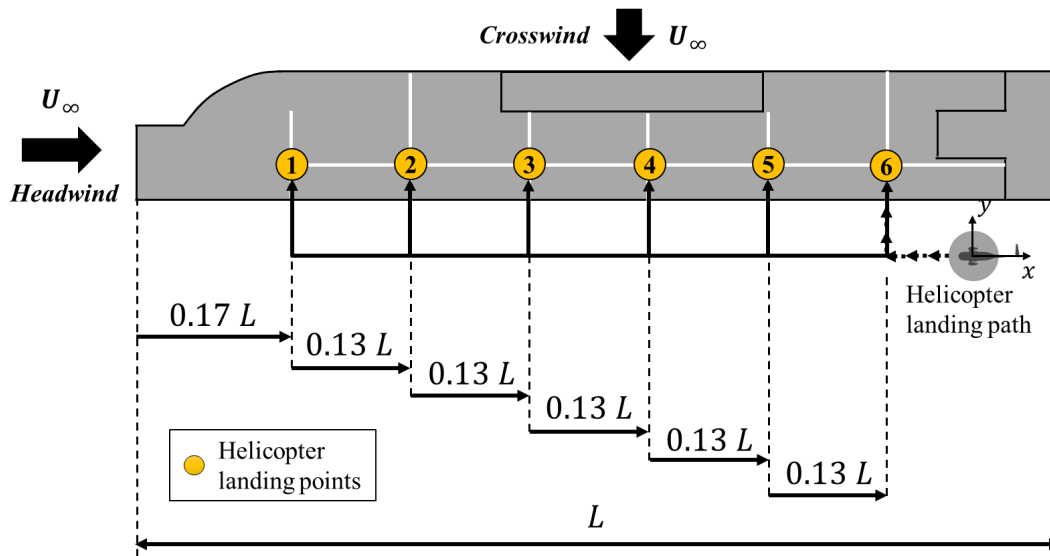

Figure 2. Helicopter landing spots on the aircraft carrier flight deck.

The structure of this paper is divided into the following sections. Section 2 describes the experimental set-up, including the wind tunnel, the Particle Image Velocimetry (PIV) system used for obtaining the results, the scaled models of aircraft carrier and helicopter used during experimental tests, and the challenges overcome to carry out the tests. Section 3 presents the results of the non-dimensional velocity contours obtained thought PIV with and without helicopter operation. Last section 4 contains the conclusions extracted from the study.

2. Experimental set-up

2.1. Wind Tunnel and Particle Image Velocimetry (PIV)

The experiments were carried out in a low-speed wind tunnel at INTA, Spain (Figure 2 a). It is a closed-circuit type and has an open and elliptical test section of 2 x 3 m². Operating at maximum power of the engine (420 kW), the airflow velocity during tests can reach up to 60 m/s with turbulence intensity below 0.5 %. The wind tunnel test section has a platform with a streamlined leading and trailing edges and that simulates the oceanic boundary layer with a calm sea state.

The wind tunnel test section is also equipped with a Particle Image Velocimetry system (PIV) [40-43] for obtaining flow visualization and non-dimensional velocity contours around the models tested.

For the proper working of the PIV (Figure 2 b), small tracer particles of ~1 μm in diameter are seeded in the flow using Laskin atomizers, and they are illuminated using two neodymium-doped yttrium aluminum garnet (Nd:YAG) pulsed lasers with a maximum energy of 190 mJ per pulse. The laser pulses are synchronized with the capture of image pairs using a digital camera with a 2048 × 2048 pixels Charged Coupled Device (CCD) sensor. As the time between the first and second image of the pair is known ($\Delta t = 25$ μs), by means of a cross-correlation process computed by a Fast Fourier Transform (FFT) algorithm, the particles displacement ($\Delta \bar{X}$) and velocity ($\bar{u}(x,t)$) can be determined in small interrogation windows of 32 × 32 pixels with a 50% window overlap following the Nyquist sampling criteria. During the tests, the field of view was 460 mm. All the velocity contours presented at the end of this study were obtained from a total of 200 averaged image pairs and plotted in non-dimensional velocity contours using Tecplot360 software.
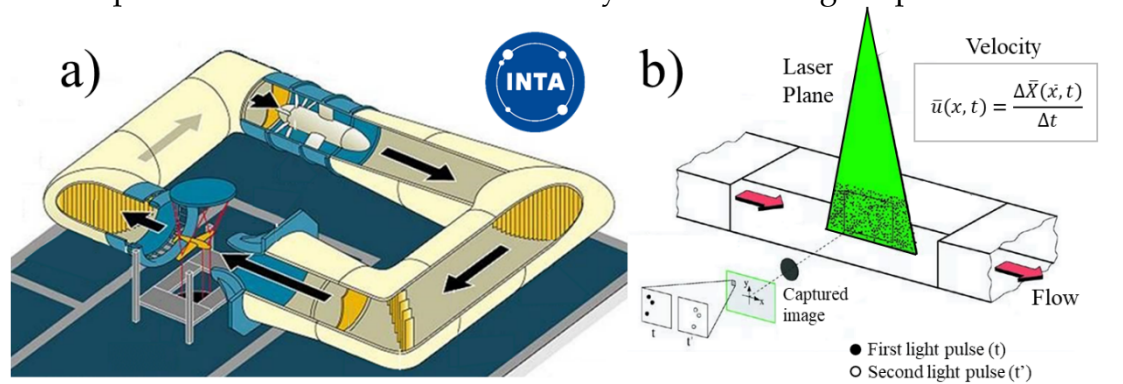

Figure 2. a) Wind Tunnel T-1 INTA and b) Particle Image Velocimetry working scheme.

2.2. Aircraft carrier scaled model

Wind tunnel tests usually requires the use of scaled models. Given the dimensions of the wind tunnel test section, and the real size of the aircraft carriers, the use of 1:100 scaled models for both helicopters and aircraft carrier was necessary. Despite the reduction in the size, the scaled models accurately replicate the original geometries, with the models manufactured by 3D printing technology. Furthermore, the velocity selected during the tests ($U_\infty = 8.5$ m/s) ensures a Reynolds number exceeding 10^5, that is the aerodynamic similarity criteria for bluff bodies.

Figure 3 displays two photographs captured during wind tunnel tests, simulating headwind and crosswind conditions with respect to the aircraft carrier and helicopter operation. As displayed, the helicopter is always oriented to the bow of the aircraft carrier.
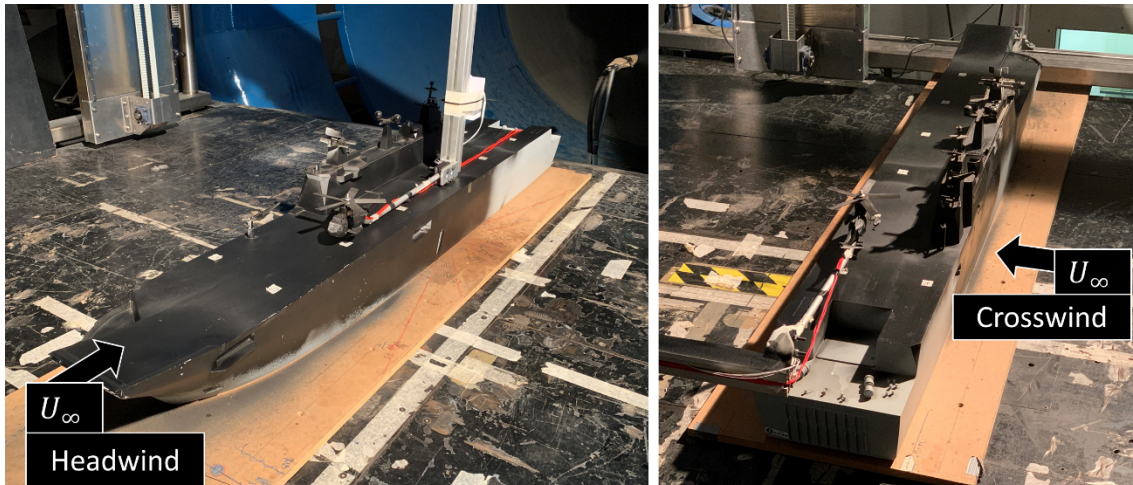
Figure 3. 1:100 scaled aircraft carrier and helicopter under headwind and crosswind conditions during wind tunnel tests.

2.3. Helicopter scaled model

The 1:100 scaled helicopter model is based on a Sikorsky SH-3 Sea King. As displayed in the scheme of Figure 4, the helicopter scaled model is equipped with a 160 mm diameter 3D printed helicopter rotor, an Axi 2204/54 brushless engine with adjustable power to regulate the revolutions of the rotor, an internal balance for six-component force measurements (HELIBAL), "Z" shaped brackets for the engine, a frame to fix all components, two half 3D printed helicopter fuselage, and a sting bar that holds the full assembly.
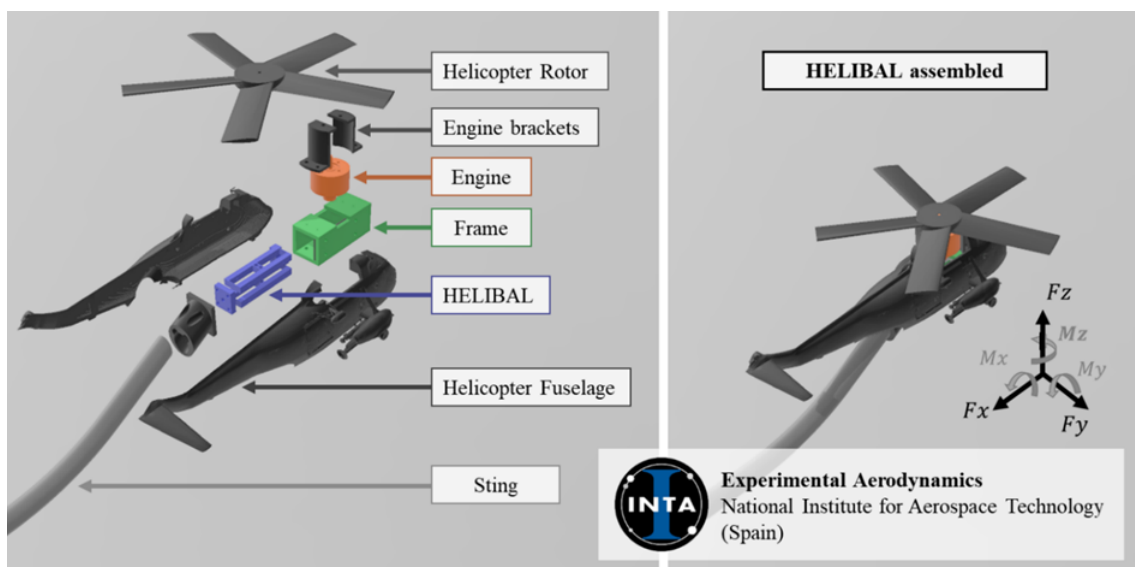

Figure 4. Scheme of the scaled helicopter model full-assembly.

The internal balance is used in these tests to monitor the thrust force generated by the model, ensuring the flow similarity between the real helicopter and the scaled model during wind tunnel tests. Ensure the rotor flow similarity means making equal the values of thrust coefficient (C_T) and advance ratio (J) of the real and scaled helicopter model. The full-scale helicopter has a thrust coefficient during hovering flight of,

$$C_T = \frac{T_{io}}{\rho(\Omega R)^2 S} = 6.47 \times 10^{-3} \qquad (1)$$

where $M = 7130$ kg, $T_{io} = W = (M \times g)$ N, $\rho = 1.225\ kg/m^3$, $\Omega = 250$ rpm, R = 8 m, $S = 201$ m^2, and $g = 9.81\ m/s^2$.

Using the 1:100 scaled model, the same value of thrust coefficient was obtained operating at 25 W (10 V and 2.5 A), resulting in a scaled rotor speed of $\Omega_s = 8,500$ rpm and a similar thrust coefficient of the model of $C_T = 6.47 \times 10^{-3}$ measured with the internal balance HELIBAL.

The similarity of the advance ratio is also achieved. The wind condition represented during the tests is a relative wind of $U_\infty = 25$ m/s, that corresponds to the navigation speed of the aircraft carrier (20 knots ~ 10 m/s) and a wind velocity of 15 m/s. As the angular velocities of the real and scaled helicopter are known $\Omega = 250$ rpm, $\Omega_s = 8,500$ rpm, and the rotor radius for the real and scaled helicopter are $R = 8$ m, and $R_s = 0.08$ m, the advance ratio similarity is also achieved when $V_{tunnel} = 8.50$ m/s,

$$J = \frac{2U_\infty}{\Omega R} = \frac{2V_{tunel}}{\Omega_s R_s} \qquad (2)$$

It is important to mention that during tests, the full assembly is attached to an automatic positioning system, to place the helicopter automatically above the landing spots of the aircraft carrier. Regardless the wind condition simulated, the helicopter always maintains a parallel orientation to the ship, aligning the pilot's view with the bow of the vessel, as presented in Figure 5.
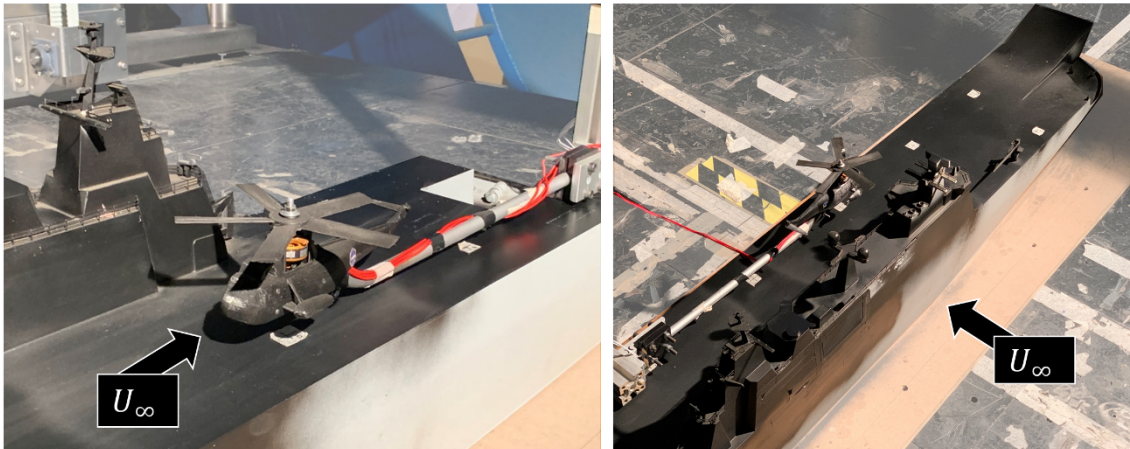

Figure 5. 1:100 scaled helicopter and aircraft carrier during the wind tunnel tests.

2.4. Challenges encountered

The experimental setup performed was not free of challenges to obtain good quality images with the PIV system. The surfaces of the aircraft carrier are close to the laser light plane of the PIV and have caused undesired reflections. For example, both the flight deck and the carrier island generated problems during PIV testing introducing light scattering on the Camera Field of view during PIV experiments (Figure 6 a). This results into original captured images with high saturation levels, making impossible to correlate the position of the seeded particles (Figure 6 b.1).
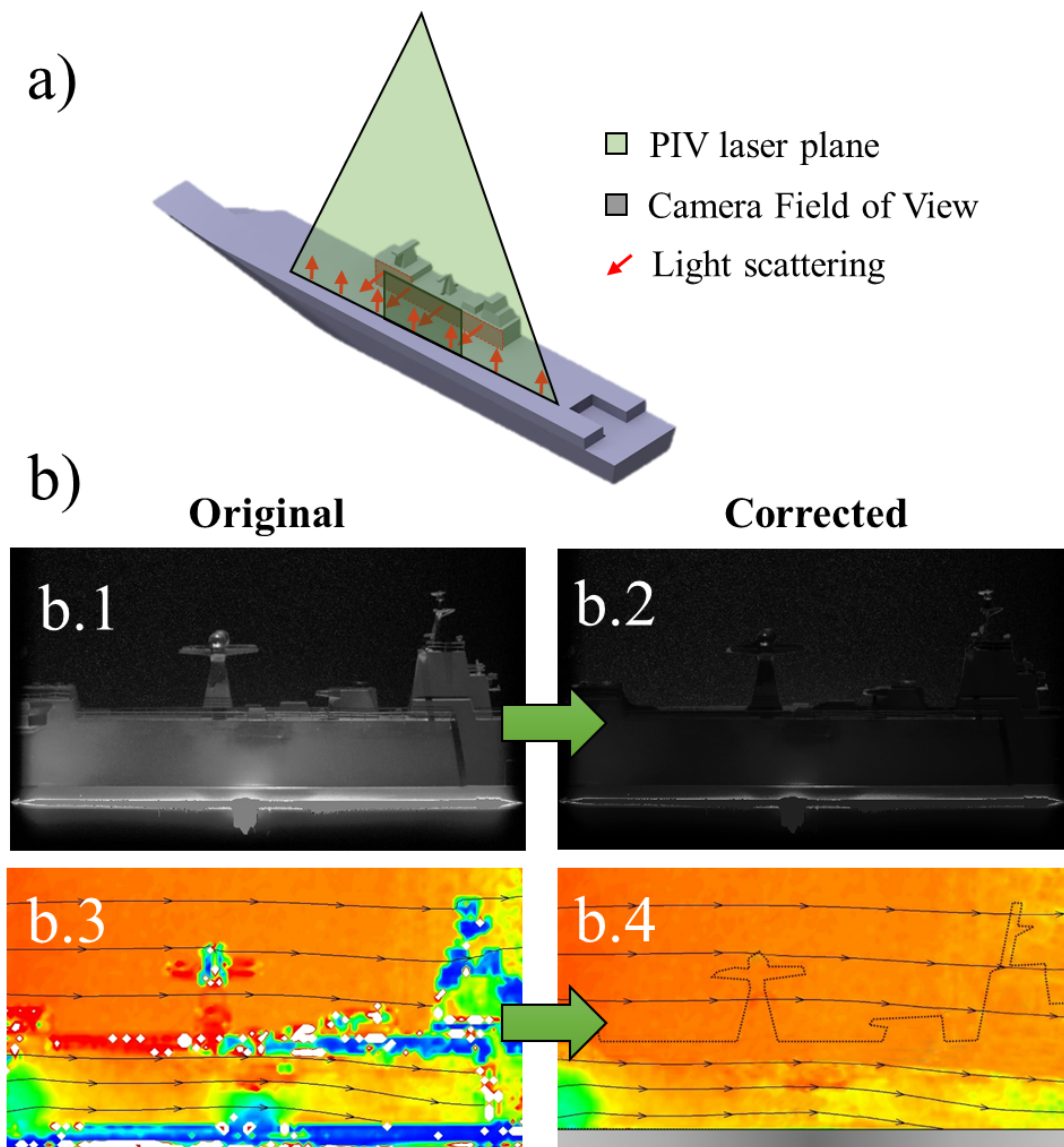
Figure 6. a) Aircraft carrier, PIV laser plane, camera field of view, and light scattering during tests. b) Differences during PIV capturing when the model is painted in black b.1 and b.2, and the resultant velocity contours b.3 and b.4.

To avoid such reflections and to be able to correctly capture the positions of the tracer particles in the images, all surfaces of the model were painted black. This way, the laser reflections and high saturation areas were minimized, obtaining better images (Figure 6 b.2) and cross-correlation results for obtaining velocity contours. Additionally, a post-processing analysis was performed by detection of vector holes caused by spurious vectors and filling them by a local mean filter of size 3 x 3. Then, following this procedure, the final velocity contours extracted from PIV were improved from the first trials (Figure 6 b.3) to the final results (Figure 6 b.4).

Likewise, the helicopter and its rotor had to be made of black PLA (Polylactic Acid) to avoid laser reflections. However, as the laser plane is shuttered from the upper part of the wind tunnel test section, the fuselage and the rotor produces shadows under them. Additionally, the problem of capturing images with PIV around the helicopter is even more challenging since there is a propeller rotating at high speed. This generates shadows and reflections, as displayed in Figure 7 a. As an example, Figure 7 b shows a velocity contour from a single frame and without post-processing, showing wrong data under the rotor and the helicopter fuselage. Figure 7 c shows the resultant velocity contour obtained from the 200 averaged image pairs captured during tests and corrected by post-processing software.
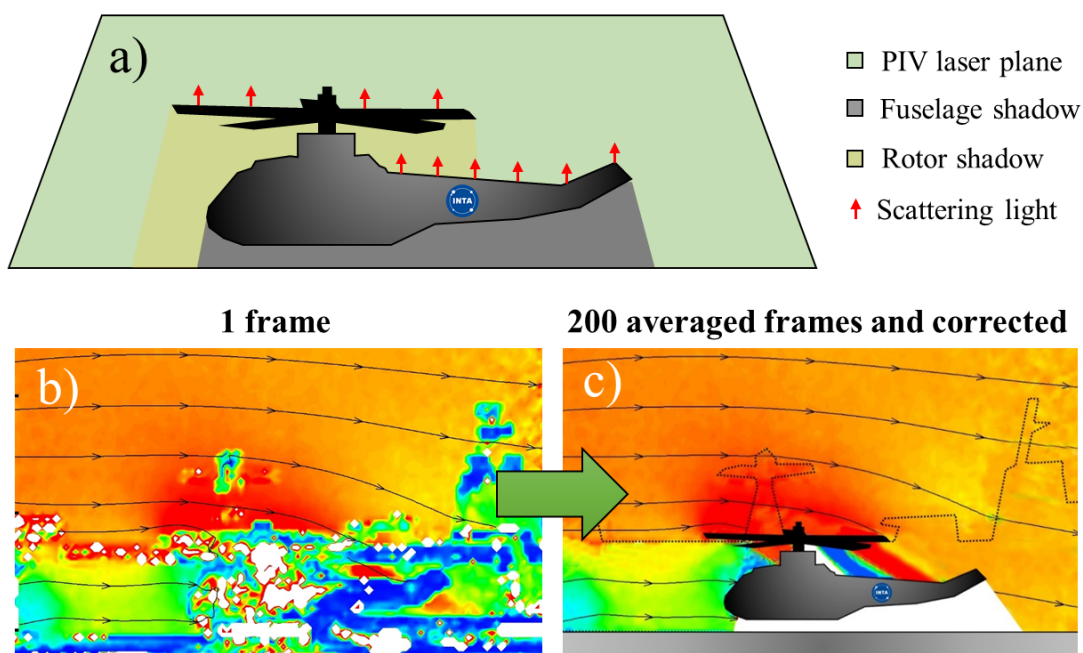
Figure 7. a) Problems with the scaled helicopter during PIV acquisition. b) Resultant velocity contour of a pair of images. c) Resultant velocity contour of 200 averaged frames.

Figure 8 explains how the shadows under the helicopter rotor can be solved. Since the rotor is in motion at a speed of 8,500 rpm, corresponding to 141.6 Hz, and the maximum capture frequency of the PIV system used is 1 Hz, it occurs that during the acquisition of 200 pairs of images the light passes through the rotor in a changing way, illuminating areas under the rotor alternately. Figure 8 a shows how the position of the rotor changes between two frames of the PIV capturing process. As an example, Figure 8 b.1 and b.2 shows the first image of the pair 31 and 32 of 200 pairs, captured with 1 second of delay. Figure 8 c.1 presents the corresponding velocity contour processed from the image pair 31. The red arrow indicates an area where information is lost under the rotor. However, image pair 32 (Figure 8 b.2) does not have these shadow. Using the 200 image pairs captured, and making the average velocity contour from them, the resultant averaged and corrected velocity contour is displayed at Figure 8 c.2.
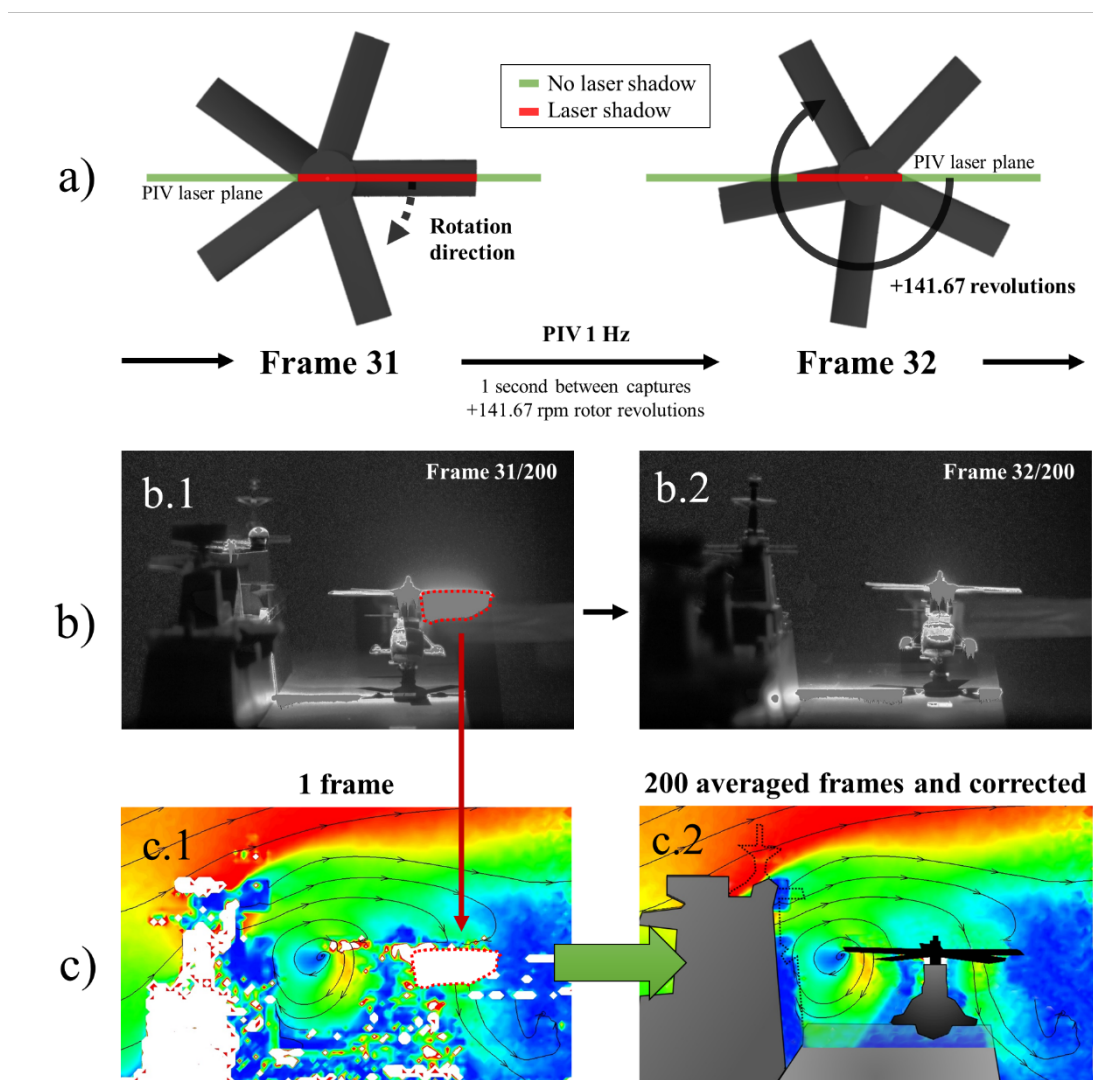
Figure 8. a) Positions of the rotor with respect to the PIV laser plane in different frames. b) Captured PIV images in frames 31 and 32 c) Comparison of velocity contours of 1 frame and 200 averaged frames and corrected.

3. Results

3.1.Headwind condition

Figures 9 and 10 show the non-dimensional velocity contours for the headwind cases without the helicopter (1 to 6) and with the helicopter operation (1H to 6H). They represent by colors the velocity magnitude from PIV, divided by the wind tunnel velocity during the tests (V/U_∞), and with the streamlines overlapped. The contours are ordered from spot 1, which is closest to the bow, to spot 6, which corresponds to the landing spot closest to the stern of the aircraft carrier. The origin of coordinates ($x = 0$ mm, $z = 0$ mm), is placed in each map at the helicopter landing spot analyzed in each case.

In Figure 9, spot 1 shows a flow over the deck disturbed in modulus and direction by the ski-jump ramp at the bow. At spot 2, there is a more uniform flow and velocities over the deck more similar to the free flow. Spot 3, however, shows some curvature of the lines and velocity changes caused by the aircraft carrier island, and also by some artifacts in the image caused by the closeness of the surfaces of the model to the laser.
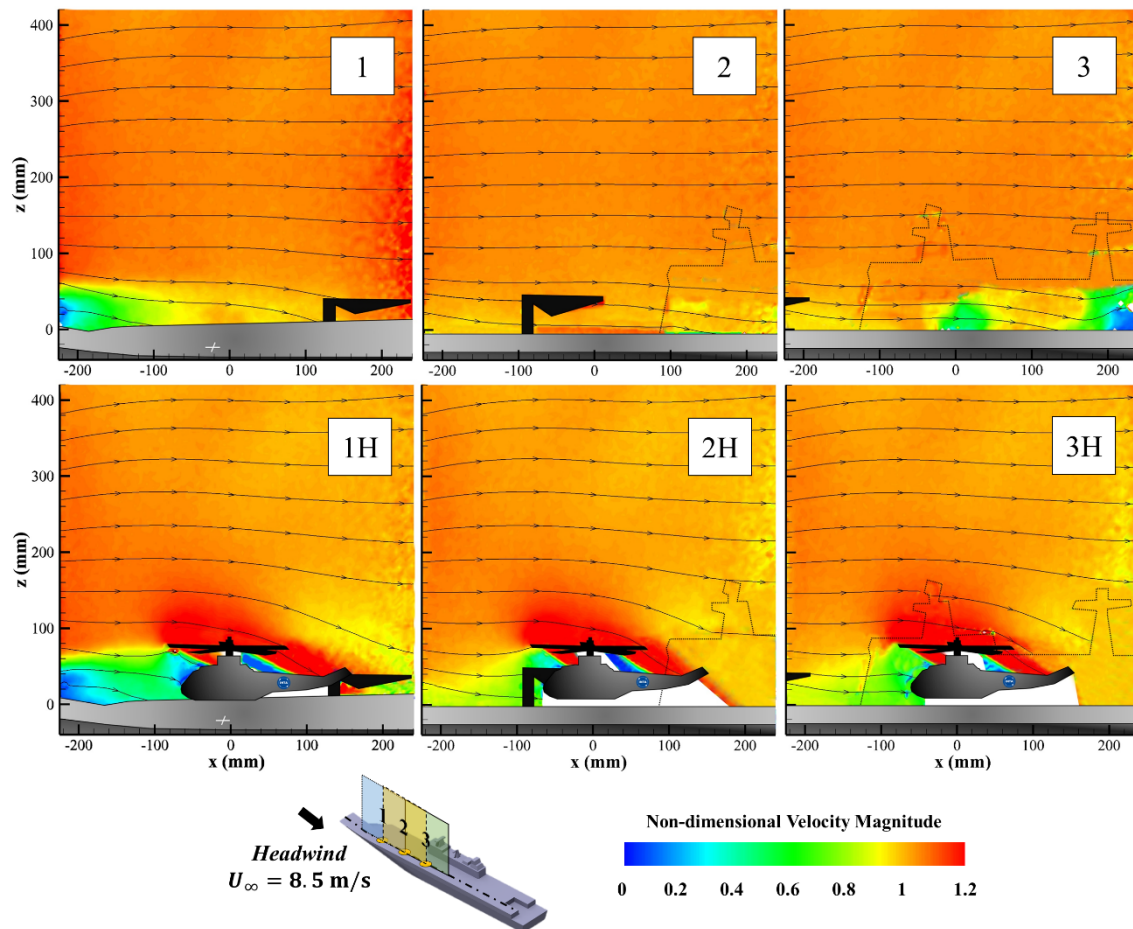
Figure 9. PIV non-dimensional velocity contours of positions 1, 2, and 3 (headwind condition).

When the operation of the helicopter is added to the problem, case 1H is clearly the most affected by the aerodynamics of the ship's bow. The incident velocities to the helicopter fuselage are lower than in the other cases. In addition, a shear layer (in yellow) also directly affects the rotor height during operation. In the 2H and 3H positions, the flow patterns with helicopter are very similar, but the incident velocities are higher at the front of the rotor than in the 1H case (due to the lower bow effect).

Figure 10 shows velocity contours without helicopter in which the flow over the deck in cases 4 and 5 is similar to that described in spot 3. Spot 6, is far from the bow and the presence of the island, and has a very uniform flow with velocities similar to the undisturbed free stream. When the helicopter is added, the effect of the ship's aerodynamics is reduced as the helicopter is placed in spots closer to the stern. Thus, the flow is more disturbed ahead of the helicopter in 4H, than in 5H or 6H, a case in which the helicopter is flying over the deck with no disturbances upstream.

In view of the results shown, headwind operation of the helicopter appears most favorable at spots 2H and 6H, which have lower disturbances generated by the bow or the island, and followed by spots 3H, 4H.
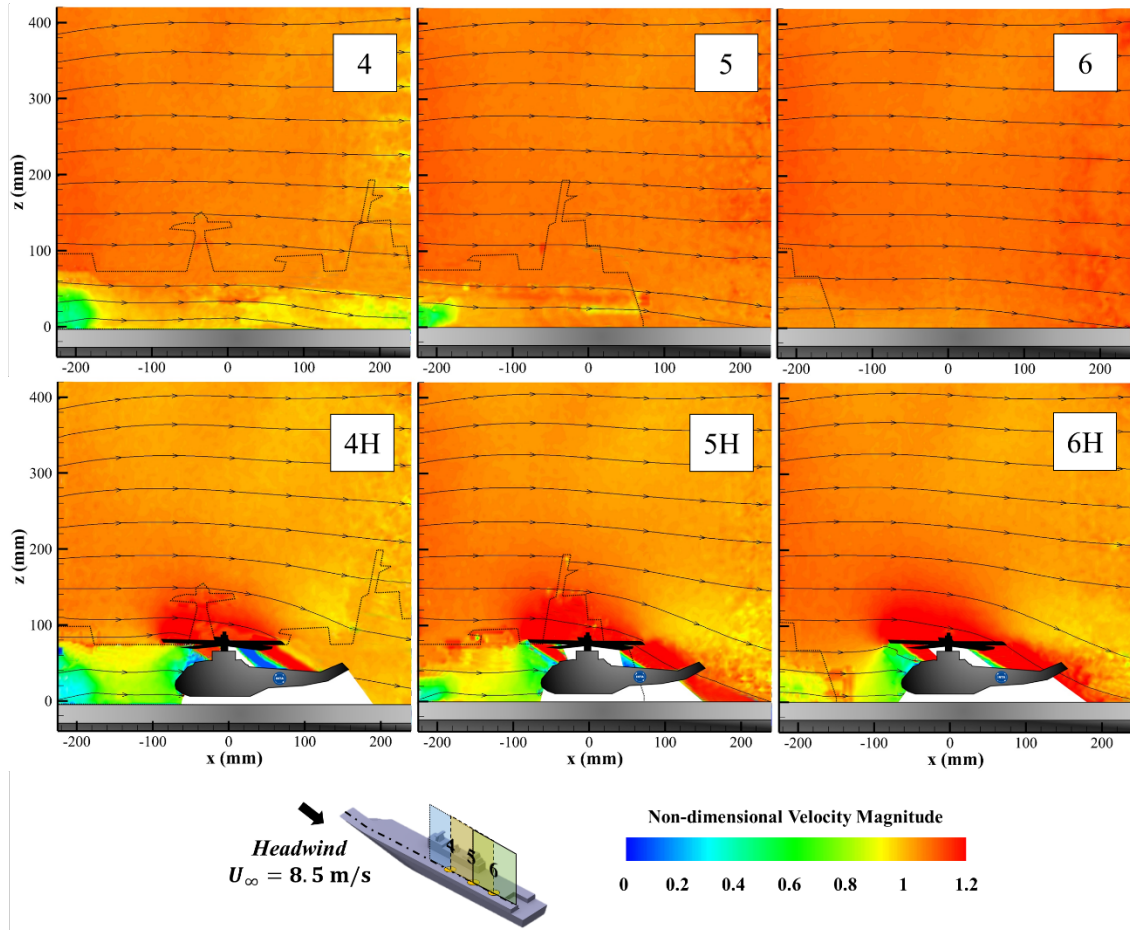
Figure 10. PIV non-dimensional velocity contours of positions 4, 5, and 6 (headwind condition).

And the helicopter landing spot with the greatest interference between the aerodynamics of the helicopter and the aircraft carrier is 1H. Among all of them, differences in incident velocity to the helicopter of up to 70 % (from 0.7 to 0.2 in non-dimensional value) can be found.

3.2. Crosswind condition

Figures 11 and 12 show the non-dimensional velocity contours for the crosswind cases. The spots are again ordered from the bow to the stern of the flight deck, and the origin of coordinates ($y = 0$ mm and $z = 0$ mm) is placed at each landing spot. Cases without helicopter are shown in contours 2 to 6, and cases with helicopter operation from 2H to 6H.
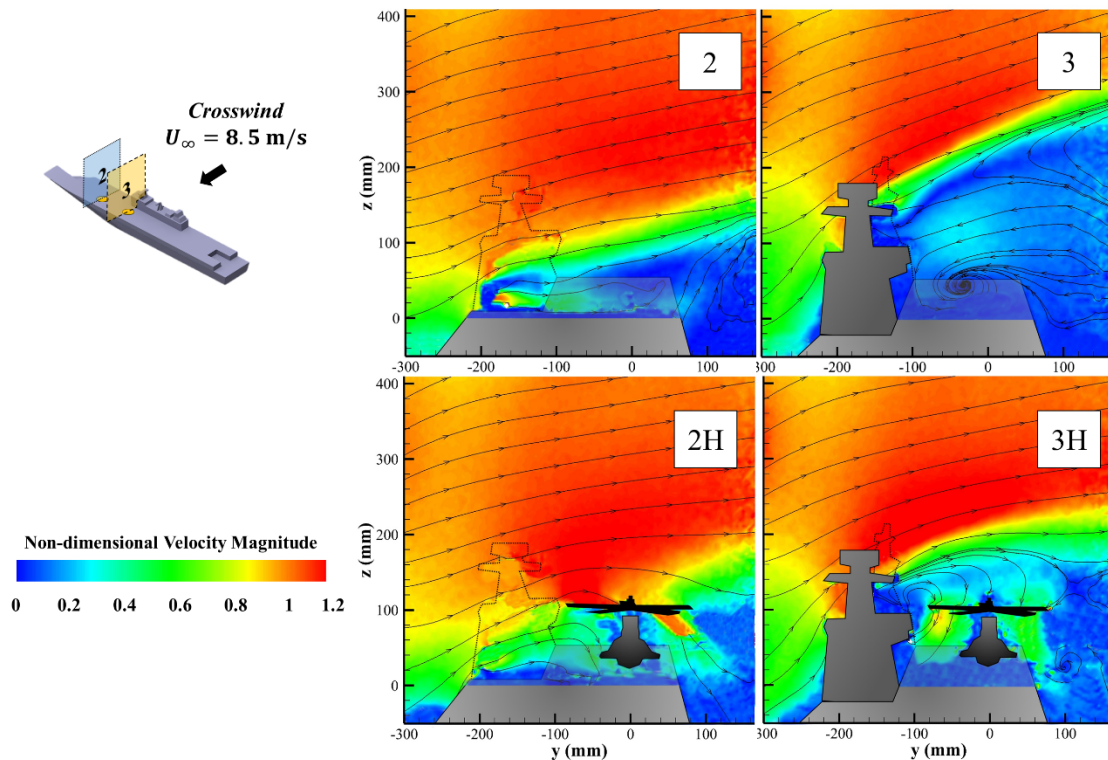
Figure 11. PIV non-dimensional velocity contours of positions 1, and 2 (crosswind condition).

Specifically, Figure 11 shows spots 2 and 3 which are located near the bow. Spot 2 shows a base flow affected by the presence of the ship's hull, which generates a zone of low velocities above the deck in which the helicopter fuselage is immersed when it is positioned over the landing spot (2H). The situation is aggravated in position 3. Here, the presence of the island generates a highly detached flow with a large zone of low velocities and a recirculation bubble in which the helicopter is completely immersed when it is placed at position 3H. In addition, spot 3 is located right next to the navigation bridge tower, which is the highest structure of the island. All this means that at this spot, rotor flow ingestion occurs at much lower speeds (- 65%) compared to the spot 2H or with the previous headwind cases seen above, and can affect helicopter stability and operation.

Figure 12 shows landing spots 4, 5, with similar flow patterns to those seen in spot 3, where the flow detachment caused by the island continues to dominate the aerodynamics. However, the height of the low velocity zone is now lower, caused by the lower height of the island next to those spots. When the helicopter is introduced at these positions (4H and 5H), low ingestion velocities are also observed, but higher than at spot 3H. Finally, at spot 6, the detachment is produced again by the incidence of the wind on the hull of the ship, and the detachment zone begins in a lower height. However, the helicopter is still completely immersed in the low speed zone (6H), which can make the operation slightly complex also at this spot.
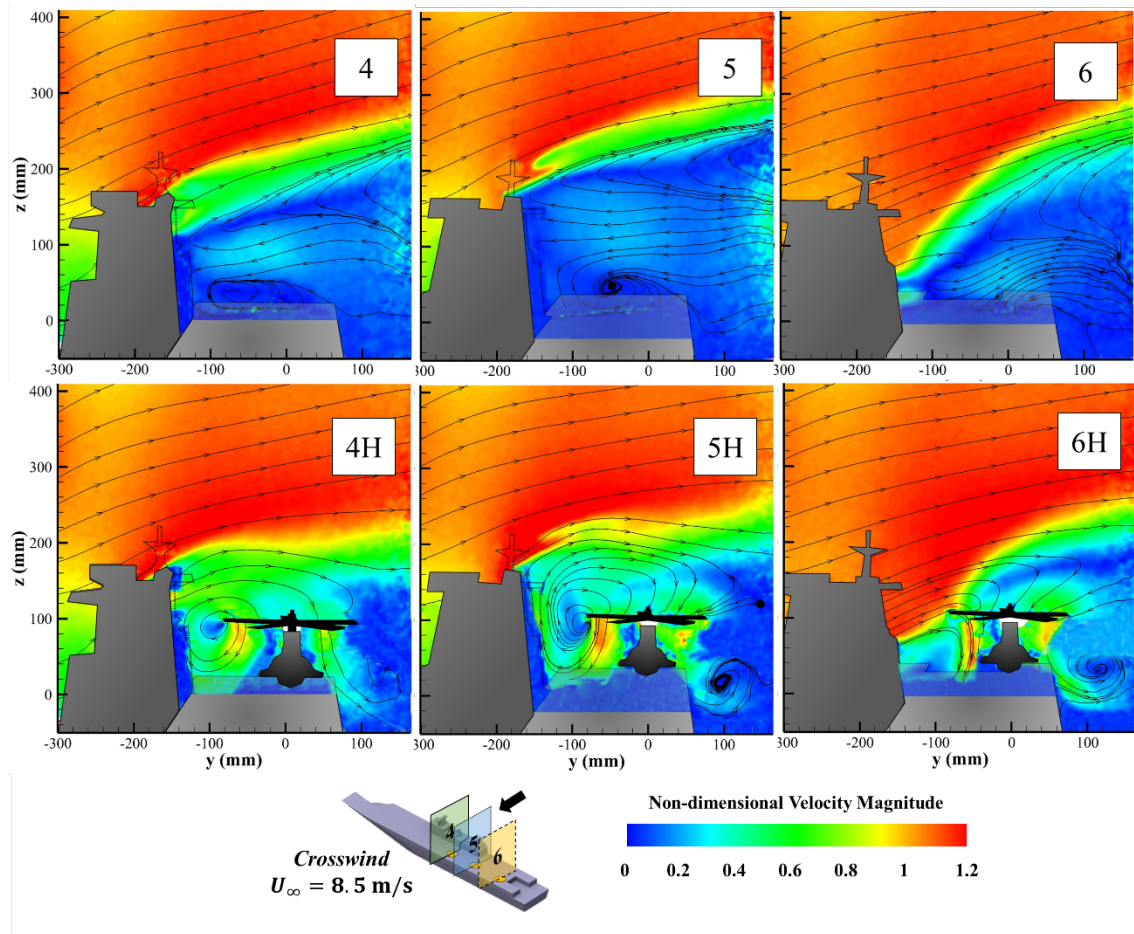
Figure 12. PIV non-dimensional velocity contours of positions 3, 4, and 5 (crosswind condition).

In this way, crosswind cases could be ordered by highest to lowest interference between helicopter and aircraft carrier flows as follows. Spot 3H presents the largest flow detachment caused by the presence of the navigation bridge, followed by the positions behind the island 4H and 5H. Finally, outside the island it has been still observed a detachment at the stern (6H) and the lowest intensity detachment near the bow (2H).

4.   Conclusions

In this paper, laser anemometry by PIV in wind tunnel has been used to analyze experimentally the aerodynamic interaction between an aircraft carrier and a helicopter operation. The experimental set-up has been described, including the scaled models and the aerodynamic similarity requirement to guarantee the validity of the tests. The results have shown non-dimensional velocity contours obtained with PIV for headwind and crosswind cases of the aircraft carrier, at different landing spots above the flight-deck. The results have allowed to describe and understand better the complex aerodynamic flow that appears close to the helicopter operating

spots over the aircraft carrier and the interaction that occurs when a full helicopter is operating over the carrier.

As a summary of the results described for both wind conditions (headwind and crosswind), Figure 13 shows a diagram with the spots analyzed, indicating by a simple color code the aerodynamic interference found between the helicopter and the aircraft carrier. Red points indicate the highest interference, orange points for medium interference and green points for the lowest interference found. Interferences have been measured through velocities around the helicopter, where there are variations of up to 70 % between the different cases tested. As expected, under headwind cases the largest interaction effects were founded at the spots near the ski-jump ramp at the bow (1) and near the island (3 and 4). In the crosswind cases, the largest effects were founded at the spots behind the island (3, 4 and 5), as a big flow detachment makes the helicopter to be immersed in a detached and turbulent area.
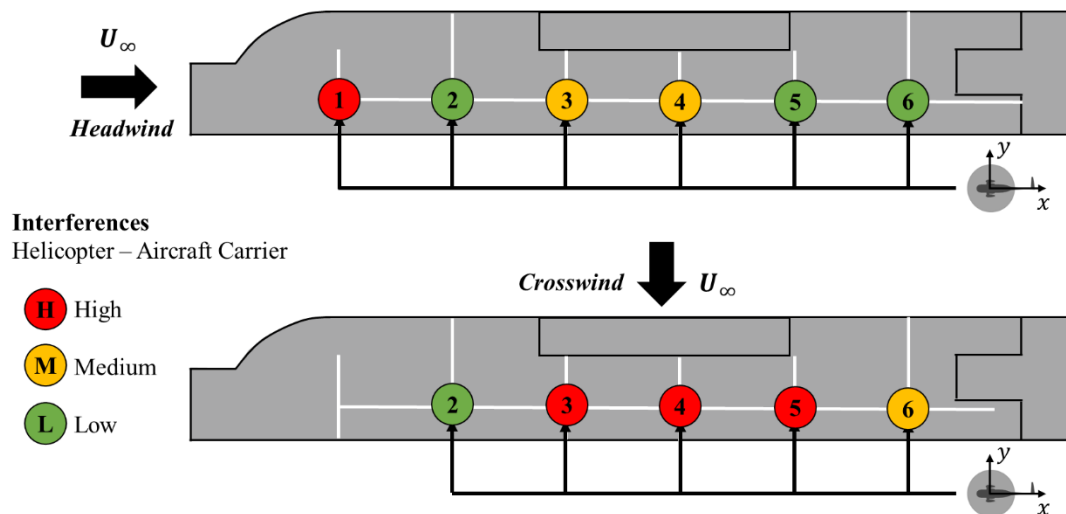

Figure 13. Interferences between helicopter and aircraft carrier aerodynamics founded.

Although the results shown help to better understand the helicopter-over-carrier coupling problem, future tests will be needed including force measurements and relating them to the possible pilot workload at each spot, in order to establish recommendations and operational limits to this kind of helicopter operations.

Acknowledgments

"Termofluidodinámica" program 464A 64 1999 14 205 0005 of the Spanish Ministry of Defense with INTA internal code IDATEC S.IGB21001.

References

[1] Łusiak, T. & Dziubinski, A., Szumański, K. "Interference between helicopter and its surroundings, experimental and numerical analysis". *Task Quarterly*. 13, 2009.

[2] Rowe S. J. "The response of helicopters to aerodynamic disturbances around offshore helidecks" *RAeS Conf. on Helicopter Operations in the Maritime Environment*. London, UK, 2001.

[3] C. H., Wang, Y., White, M. D., and Owen, I., "An experimental technique for evaluating the aerodynamic impact of ship superstructures on helicopter operations," *Ocean Engineering*, vol. 61, 2013, pp. 97–108. doi: 10.1016/j.oceaneng.2012.12.052

[4] Bardera-Mora, R., León Calero, M., and García-Magariño, A., "Aerodynamic effect of the aircraft carrier island on flight deck flow with Cross Wind," *Proceedings of the Institution of Mechanical Engineers*, Part M: Journal of Engineering for the Maritime Environment, vol. 232, 2017, pp. 145–154. doi: 10.1177/1475090216689172

[5] Lee, R. and S. Zan. 2005. Wind Tunnel Testing of a Helicopter Fuselage and Rotor in a Ship Airwake. *Journal of the American Helicopter Society*. 50(4):326-337.

[6] Lee, R. G., and Zan, S. J., "Unsteady aerodynamic loading on a helicopter fuselage in a ship Airwake," *Journal of the American Helicopter Society*, vol. 49, 2004, pp. 149–159. doi: 10.4050/jahs.49.149

[7] Healey, J. Val., "Establishing a database for flight in the wakes of structures," *Journal of Aircraft*, vol. 29, 1992, pp. 559–564.

[8] Dooley, G. M., Krebill, A. F., Martin, J. E., Buchholz, J. H. J., and Carrica, P. M., "Structure of a Ship Airwake at Multiple Scales," *AIAA Journal*, Vol. 58, No. 5, 2020, pp. 2005–2013. doi: 10.2514/1.J058994

[9] Thedin, R., Murman, S., Horn, J., and Schmitz, S., "Effects of Atmospheric Turbulence Unsteadiness on Ship Airwakes and Helicopter Dynamics," *Journal of Aircraft*, Vol. 57, No. 3, 2020, pp. 534–546. doi: 10.2514/1.C035643

[10] Yuan, W., Wall, A., & Lee, R. (2018). "Combined numerical and experimental simulations of unsteady ship airwakes". *Computers & Fluids*, 172, 29-53.

[11] Crozon, C., Steijl, R., and Barakos, G. N., "Numerical Study of Helicopter Rotors in a Ship Airwake," *Journal of Aircraft*, Vol. 51, No. 6, 2014, pp. 1813–1832. doi: 10.2514/1.C032535

[12] Brownell, C., L. Luznik, M. Snyder, H. Kang and C. Wilkinson. 2012. "In Situ Velocity Measurements in the Near-Wake of a Ship Superstructure". *Journal of Aircraft*. 49(5):1440-1450.

[13] Bardera, R., "Flow field velocity on the flight deck of a frigate," *Proceedings of the Institution of Mechanical Engineers, Part G: Journal of Aerospace Engineering*, vol. 228, 2014, pp. 2674–2680.

[14] Bardera-Mora, R., Barcala-Montejano, M., Rodríguez-Sevillano, A., de Diego, G., & de Sotto, M. (2015). "A spectral analysis of laser Doppler anemometry turbulent flow measurements in a ship air wake". *Proceedings Of The Institution Of Mechanical Engineers, Part G: Journal Of Aerospace Engineering*, 229(12), 2309-2320.

[15] Van Muijden, J., Boelens, O., van der Vorst, J., and Gooden, J., "Computational Ship Airwake Determination to Support Helicopter-Ship Dynamic Interface Assessment," *21st AIAA Computational Fluid Dynamics Conference*, AIAA Paper 2013-3078, 2013.doi: 10.2514/6.2013-3078

[16] Wakefield, N. H., Newman, S. J., and Wilson, P. A., "Helicopter Flight Around a Ship's Superstructure," *Proceedings of the Institution of Mechanical Engineers, Part G: Journal of Aerospace Engineering*, Vol. 216, No. 1, 2002, pp. 13–28. doi: 10.1243/0954410021533391

[17] Wadcock, A. J., G. K. Yamauchi, J. T. Heineck, M. J. Silva and K. R. Long. "PIV Measurements of the Wake of a Tandem-Rotor Helicopter in Proximity to a Ship". *National Aeronautics and space administration* moffett field CA AMES research center. 2004

[18] Doane, S. R. and D.A. Landman. 2012. "A wind tunnel investigation of ship airwake/rotor downwash coupling using design of experiments methologies". In: P*roceedings of the 50th AIAA Aerospace Sciences Meeting including the New Horizons Forum and Aerospace Exposition*. 2012-0767.

[19] Silva, Mark J. Yamauchi, Gloria K. Wadcock, Alan J. Long, Kurtis R., "Wind tunnel investigation of the aerodynamic interactions between helicopter and tilt-rotors in a shipboard environment". *American Helicopter Society 4th Decennial Specialist's Conf. on Aeromechanics*, San Francisco, CA, 2004.

[20] Derby, M., and Yamauchi, G., "Design of 1/48th-scale models for ship/rotorcraft interaction studies," *21st AIAA Applied Aerodynamics Conference*, 2003. doi: 10.2514/6.2003-3952

[21] Wang, Y., Curran, J., Padfield, G. D., and Owen, I., "AirDyn: An instrumented model-scale helicopter for measuring unsteady aerodynamic loading in airwakes," *Measurement Science and Technology*, vol. 22, 2011, p. 045901. doi: 10.1088/0957-0233/22/4/045901

[22] Kääriä, C. H., Forrest, J. S., and Owen, I., "The virtual airdyn: A simulation technique for evaluating the aerodynamic impact of ship superstructures on helicopter operations," *The Aeronautical Journal*, vol. 117, 2013, pp. 1233–1248. doi: 10.1017/s0001924000008836

[23] Taymourtash, N., Zanotti, A. Gilbertini, G. Quaranta, G. "Simulation and Testing of Helicopter-ship Aerodynamic Interaction". *47th European Rotorcraft Forum*, Glasgow, Scotland, 7-9 September, 2021.

[24] Thedin, R., Kinzel, M. P., Horn, J. F., and Schmitz, S., "Coupled Simulations of Atmospheric Turbulence-Modified Ship Airwakes and Helicopter Flight Dynamics," *Journal of Aircraft*, Vol. 56, No. 2, 2019, pp. 812–824. doi: 10.2514/1.C035158

[25] Memon,W. A., Owen, I., and White, M. D., "Motion Fidelity Requirements for Helicopter-Ship Operations in Maritime Rotorcraft Flight Simulators," *Journal of Aircraft*, Vol. 56, No. 6, 2019, pp. 2189–2209. doi: 10.2514/1.C035521

[26] Watson, N. A., Owen, I., and White, M. D., "Piloted Flight Simulation of Helicopter Recovery to the Queen Elizabeth Class Aircraft Carrier," *Journal of Aircraft*, Vol. 57, No. 4, 2020, pp. 742–760. doi: 10.2514/1.C035733

[27] Forrest, J., Kaaria, C., and Owen, I., "Evaluating Ship Superstructure Aerodynamics for Maritime Helicopter Operations Through CFD and Flight Simulation," *Aeronautical Journal*, Vol. 120, No. 1232, 2016, pp. 1578–1603. doi: 10.1017/aer.2016.76

[28] Forsythe, J., Lynch, E., Polsky, S., and Spalart, P., "Coupled Flight Simulator and CFD Calculations of Ship Airwake Using Kestrel," *53rd AIAA Aerospace Sciences Meeting*, AIAA Paper 2015-0556, 2015.doi: 10.2514/6.2015-0556

[29] Foeken, M. Pavel, M. D. "Investigation on the simulation of helicopter/ship operations". *Faculty of Aerospace Engineering*, Delft University of Technology Kluyverweg 1, 2629 HS, Delft, The Netherlands.

[30] Mehling, T., Halbe, O., Gasparac, T., Vrdoljak, M., and Hajek, M. "Piloted Simulation of Helicopter Shipboard Recovery with Visual and Control Augmentation". *In AIAA Scitech 2021 Forum*. 2021. doi: 10.2514/6.2021-1136

[31] Kumar, K Vignesh & Marthamootil, Mathew & Singh, Sidh & Sinha, Sawan & Vijayakumar, R. "Experimental investigation of flow over the flight deck of a generic aircraft carrier." *Warship 2018 - Procurement of Future Surface Vessels*, Royal Institution of Naval Architects, UK

[32] Watson, N. A., Kelly, M. F., Owen, I., Hodge, S. J., and White, M. D., "Computational and experimental modelling study of the unsteady airflow over the aircraft carrier HMS queen Elizabeth," *Ocean Engineering*, vol. 172, 2019, pp. 562–574. doi: 10.1016/j.oceaneng.2018.12.024

[33] Bardera-Mora R., Barcala-Montejano M. A., Rodríguez-Sevillano A., Nova-Trigueros J., "Passive flow control over the ski jump of aircraft carriers." *Ocean Engineering*, 114. 2016 pp. 134-141. Elsevier, Ltd.

[34] Ryan and M. Cummings, "A Systems Analysis of the Introduction of Unmanned Aircraft Into Aircraft Carrier Operations", IEEE Transactions on Human-Machine Systems, vol. 46, no. 2, pp. 209-220, 2016. Available: 10.1109/thms.2014.2376355.

[35] A. Fry, R. Cook and N. Revill, "CVF ski jump ramp profile optimization for F-35B", The Aeronautical Journal, vol. 113, no. 1140, pp. 79-85, 2009. Available: 10.1017/s0001924000002803.

[36] Bardera, Rafael, Garcia-Magariño, Adelaida, Rodriguez-Sevillano, Angel, Barcala-Montejano, Miguel. (2018). Aerodynamic Flow Effects on Aircraft Carrier Takeoff Performance. 2019 Journal of Aircraft 56 (3); pp. 1005-1013 doi: 10.2514/1.C035188

[37] Bardera, R., and Matías-García, J. C., "Optimization of passive flow control above the ski jump ramp of an aircraft carrier by CFD and experimental investigation," *Ocean Engineering*, vol. 263, 2022, p. 112419.doi: 10.1016/j.oceaneng.2022.112419

[38] Matías, J. C., Bardera, R., Franchini, S., Barroso, E., and Sor, S., "A comparative analysis of helicopter recovery maneuvers on a SFS by means of PIV and balance measurements," *Ocean Engineering*, vol. 275, 2023, p. 114119. doi: 10.1016/j.oceaneng.2023.114119

[39] Matias-Garcia, J. C., Bardera, R., Franchini, S., Barderas, E. B., and Sor, S., "Design and integration of an internal balance prototype for wind tunnel tests of a scaled helicopter model," *AIAA AVIATION 2023 F*orum, 2023.doi: 10.2514/6.2023-3536

[40] Raffel, M., Willert, C. E., Scarano, F., Kähler, C. J., Wereley, S. T., and Kompenhans, J., *Particle image velocimetry: A practical guide*, Cham: Springer International Publishing, 2018.

[41] Adrian, R. J., and Westerweel, J., *Particle image velocimetry, Cambridge*: Cambridge University Press, 2011.

[42] Prasad, A. K. "Particle image velocimetry". *Current science-bangalore*, 79(1), 51-60, 2000.

[43] Adrian, R. J., "Particle-imaging techniques for Experimental Fluid Mechanics," *Annual Review of Fluid Mechanics*, vol. 23, 1991, pp. 261–304. doi: 10.1146/annurev.fl.23.010191.001401